LANGMUIR

pubs.acs.org/Langmuir Article

Molecular Dynamics Study of Bubble Nucleation on Grooved Surfaces with Instantaneous Substrate Heating Using a Pressure-Control Method

Ziqi Li, Ziqi Cai,* Zhengming Gao,* and Jacobus Johannes Derksen

Cite This: *Langmuir* 2026, 42, 7212−7227 Read Online

ACCESS | Metrics & More | Article Recommendations | Supporting Information

ABSTRACT: Molecular dynamics simulations were performed to investigate argon bubble nucleation under instantaneous platinum substrate heating, with a pressure-control method. The simulation starts from an equilibrium system consisting of saturated liquid/vapor argon at 90 K. A constant pressure is applied to the pressure-control plate located above the fluid to maintain the target system pressure. At time zero, the substrate temperature is instantaneously increased from 90 K to the target value, while the pressure remains fixed. The substrate temperature ranges from 130 to 150 K, and the system pressure ranges from 2 to 30 atm. Results show that higher substrate temperatures reduce critical nucleation volume and accelerate nucleation, whereas higher pressures enlarge critical nucleation volume and prolong nucleation. Within the substrate temperature and system pressure range, temperature−pressure maps reveal three regimes: low-temperature non-nucleation, intermediate pressure-sensitive transition, and high-temperature easier nucleation. The nucleation time varies from 1 to 15 ns, and the critical nucleation volume from 1 nm^3 to 9 nm^3. These findings clarify the combined effects of temperature and pressure on bubble nucleation, providing further insights into the thermal management in rapid, localized heating systems with a fluid film.

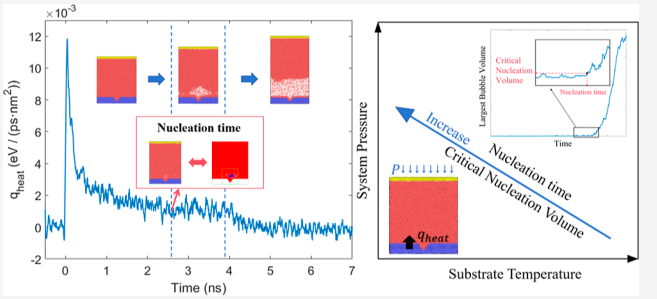

Downloaded via UNIV OF ABERDEEN on March 18, 2026 at 11:12:30 (UTC).
See https://pubs.acs.org/sharingguidelines for options on how to legitimately share published articles.

INTRODUCTION

Bubble nucleation is a fundamental phenomenon and it occurs widely in both natural settings and engineering systems. During boiling heat transfer, the nucleation and departure of bubbles can significantly enhance heat flux, forming the core mechanism behind high heat-flux heat exchangers, electronic chip cooling, and spray cooling technologies.[1,2] In cavitation and liquid transport systems, bubbles generated and collapsed may cause equipment wear, vibration, and energy losses, thereby affecting the performance and safety of key devices such as pumps, propellers, and hydraulic circuits.[3,4] In polymer processing and devolatilization during polymerization reactions, the generation and release of bubbles directly determine the product morphology and devolatilization efficiency, serving as a critical aspect of process control in extrusion and injection molding.[5,6] Additionally, in nanomaterial synthesis and biomedical microbubble technologies, nucleation processes are deliberately employed to construct nanostructures or achieve controlled drug release.[7−9] Hence, gaining a better understanding of bubble nucleation might help improve heat and mass transfer, process control, and the performance of many systems.

Early studies on bubble nucleation were primarily based on Classical Nucleation Theory (CNT), originally proposed by Volmer[10], Farkas[11] and Becker.[12] CNT relies on thermodynamic fluctuation models to predict nucleation rates and critical nucleus sizes, providing an important theoretical framework for understanding phase transitions at the macroscopic scale. With the advancement of experimental techniques, particularly the application of atomic force microscopy (AFM)[13−15] and other high-resolution measurement methods,[16,17] a growing number of experiments have directly confirmed the existence of surface nanobubbles on solid substrates, while simultaneously revealing significant discrepancies between experimental observations and CNT predictions.[18,19]

Fundamentally, CNT calculates the free energy of cluster formation using macroscopic thermodynamic parameters, whereas nucleation actually occurs at the molecular scale, typically involving structures only a few nanometers in size. Consequently, the direct extrapolation of macroscopic theories to the nanoscale inevitably limits their validity. Moreover, although experimental methods can directly capture nucleation and bubble dynamics, they remain constrained by spatial resolution, temporal resolution, and experimental controll-

Received: November 23, 2025
Revised: February 28, 2026
Accepted: March 1, 2026
Published: March 4, 2026

ACS Publications © 2026 American Chemical Society

https://doi.org/10.1021/acs.langmuir.5c06175
Langmuir 2026, 42, 7212−7227

ability, making it difficult to resolve the underlying molecular-scale mechanisms of nucleation, such as local density fluctuations, interfacial structural evolution, and solid−liquid thermal coupling.

In this context, molecular dynamics (MD) simulations have become a powerful tool for investigating bubble nucleation at the nanoscale. Compared with traditional theories and experiments, MD offers higher spatial and temporal resolution and enables precise control over temperature, pressure, surface structure, and wettability, allowing direct observation of microscopic nucleation pathways and interfacial dynamics. In this way, MD bridges the gap between classical theory and experimental observations at the molecular level. For instance, the combined experimental and numerical study by Qiu and Zhang[20] demonstrated that bubble nucleation time decreases with increasing heat flux and increases with rising system pressure, with excellent agreement between experimental and computational results, thereby validating the physical soundness and reliability of molecular-scale simulations in describing pressure−temperature coupled nucleation dynamics.

Current molecular dynamics studies on bubble nucleation mostly employ argon as the fluid. Argon can be accurately described by the widely used Lennard-Jones (LJ) potential and is therefore extensively applied in molecular dynamics simulations of fluid flow and phase change processes.[21−28] Researches have mainly explored the influence of surface structure, wettability, liquid film thickness, nanoparticles, wall temperature, and system pressure on bubble nucleation and boiling behavior.

Regarding surface nanostructures, early works paid more attention to the effect of nanostructure shape on boiling heat transfer. Rectangular nanostructure is commonly used in nanoscale boiling heat transfer. Zhou et al.[29] investigated the effects of rectangular nanostructure width on boiling and demonstrated that rectangular nanocavities significantly reduce time and wall superheat required for the onset of nucleate boiling and Cu wall superheat required for Ar nucleate boiling compared with the plain substrate. Wang[30] et al. and Zhou[22] et al. studied the impact of rectangular cavity depth and nanostructure height of Al and Cu substrate on Ar boiling heat transfer, showing that increased height improves boiling efficiency. Beyond simple rectangular geometries, others[31−33] compared the effect of nanostructures such as rectangular, spherical, conical, trapezoidal, finger and T-shaped on boiling heat transfer. For example, Liu et al.[34] investigated various groove geometries of Cu substrate and found that greater surface area enhances water molecule adsorption and interfacial interaction energy, reducing thermal resistance.

The introduction of nanoparticles is also an effective approach to further enhance boiling heat transfer since nanoparticles can act as additional heat sources and transfer energy to the liquid film, similar to nanostructures.[35−37] For instance, Yin et al.[38] studied Ar/Cu system and Wang et al. studied water/graphene system[39] and both showed that nanoparticles act as heat sources and transfer energy to liquid films, and larger particles result in higher heat transfer efficiency.

Surface wettability has also been recognized as a critical factor governing nucleation dynamics by affecting liquid film morphology and thermal resistance distribution. Wang et al.[40] found that under the same superheat, hydrophilic Au surfaces exhibit faster explosive water boiling than hydrophobic ones due to lower Kapitza resistance. Subsequently, the mixed-wettability surface is proposed to combine the advantages of hydrophobicity and hydrophilicity with the aim of improving boiling performance. Li et al.[23] demonstrated that on hybrid-wettability Pt surfaces, increasing hydrophobicity enhances cavity formation probability, while hydrophilicity accelerates Ar bubble growth. Recently, smart materials with wettability response have attracted the attention of numerous industrial fields, and surface wettability can be altered by external stimuli, including temperature, electric field, light, force, and even gas.[41−43] Deng et al.[24] showed that thermally responsive Cu surfaces combining hydrophobic and hydrophilic properties improve both Ar evaporation rates and heat flux. Overall, these studies show the significance of surface wettability in affecting the bubble nucleation and boiling heat transfer.

Different from the macroscopic scale, liquid film thickness plays a critical role in boiling heat transfer at the nanoscale. In principle, the liquid film thickness can determine the phase transition mode.[44] Wang et al.[25] found that for both hydrophilic and hydrophobic Pt surfaces, the onset temperature of explosive Ar boiling is closely related to initial film thickness and decreases with increasing thickness. Other works have obtained similar results,[45,46] showing that thin liquid films tend to evaporate completely before bubble nucleation under high heat flux, while thicker films enable bubble formation and explosive boiling. In addition, Bai et al.[47] reported that water temperature and the onset time of rapid boiling are promoted by reducing the liquid film thickness on the Cu substrate.

In terms of wall temperature, increasing thermal input generally promotes bubble nucleation and growth by enhancing energy transfer across the solid−liquid interface. Liu et al.[48] reported that the higher the Al wall temperature, the faster H_2 bubbles grow. As the heating time increases, the number of bubbles continues to rise, and eventually the bubble formation process reaches a steady state. Similar trends were observed in boiling simulations on copper surfaces. Ilic et al.[49] and Zhao et al.[50] simulated boiling on Cu surfaces and found that wall temperature rise enhances heat transfer from Cu substrate to water, thereby intensifying the boiling process. In addition to promoting heat transfer, increasing temperature can also affect the phase change mode.[51,52] Tang et al.[53,54] studied the phase change of argon atoms over solid copper wall at a constant temperature of 130 and 170 K, where evaporation and rapid boiling occur, respectively.

Regarding pressure effects, system pressure is a key thermodynamic variable governing bubble nucleation and boiling heat transfer. However, most existing molecular dynamics studies employ fixed-volume models, typically using a fixed cooling wall or a reflecting wall at the top of the domain.[30,55−57] While such setups can preserve sufficient vapor space and prevent mass and energy loss, they intrinsically constrain the pressure evolution during rapid heating. As a result, the vapor pressure may deviate substantially from physically realistic conditions in nonequilibrium boiling, which can in turn alter the driving force for nucleation, bubble growth dynamics, and interfacial heat transfer. This methodological limitation raises questions about whether conclusions drawn from fixed-volume simulations can be directly generalized to practical boiling systems, where pressure is not constrained in this manner. Therefore, rather than treating pressure as a passive or secondary parameter, the present work focuses on systematically examining bubble nucleation and boiling behavior under well-defined constant-pressure conditions. Shahmardi et al.[58] used a 1 bar pressure-controlled system to

https://doi.org/10.1021/acs.langmuir.5c06175
Langmuir 2026, 42, 7212−7227

show that surface nanostructure and wettability jointly influence water bubble nucleation, growth, and vapor film formation, with nanostructures delaying vapor film formation and enhancing energy transfer. Guo et al.[26] employed an Ar/Cu system under a pressure-controlled condition of 1 bar and showed that the nucleation rate increased with decreasing contact angle, indicating a coupling effect between wettability and pressure. Chen et al.[27] developed a modified Lennard-Jones (L-J) potential model for Ar/Pt systems with a moving plate controlling pressure of 1 atm and found that evaporation occurred at a heat source temperature of 85 K, whereas bubble nucleation was observed when the temperature was increased to 90 K. Although these studies adopted constant-pressure conditions, most of them treated pressure largely as a secondary control parameter, primarily focusing on the effects of surface nanostructure, wettability, or modified interatomic potentials on nucleation behavior. Similarly, Deng et al.[59] compared nucleate boiling characteristics of CO_2 and CO_2/PEC4 mixtures under constant-pressure (1.5 MPa) and nonconstant-pressure conditions, but their discussion was mainly limited to the differences between these two pressure-control modes. Consequently, the intrinsic mechanisms by which pressure influences nucleation dynamics warrants further research.

In this context, Hu et al.[28] advanced this line of inquiry by systematically examining the influence of different Ar/Cu system pressures on nucleate boiling, revealing that increasing pressure generally led to slower bubble growth. Lin et al.[60] also conducted a systematic MD study on R1336mzz(Z) nanofilm under pressures from 0.5 to 8 atm, demonstrating that external pressure strongly affects nucleation and bubble growth, with 1 atm yielding the fastest nucleation. Hu et al.[28] mainly compared different pressures along a single heating trajectory, whereas Lin et al.[60] essentially varied pressure at an approximately fixed wall temperature; neither study systematically investigated pressure effects across multiple temperatures nor constructed a comprehensive temperature−pressure parameter space.

Despite the breadth of studies on individual thermal factors, research on bubble nucleation under transient heating and variable pressure remains insufficient. In many micro/nanoscale scenarios—such as localized overheating in high-heat-flux microchips,[61−63] femtosecond laser material processing,[64−66] and photothermal therapy[67−69]—surface temperatures may rise abruptly within subnanosecond time scales due to high-frequency heating, laser pulses, or rapid energy deposition. Such extreme nonequilibrium thermal conditions often trigger intense phase transitions, where bubble nucleation plays a pivotal role in governing energy release, phase change, and mass/heat transfer efficiency.

Therefore, under such transient heating scenarios, the triggering mechanisms and evolution characteristics of bubble nucleation is essential for optimizing process performance. Temperature and pressure, as key thermophysical parameters, directly determine whether bubbles can be effectively initiated, grow sustainably, and remain stable, ultimately influencing the system's heat transfer efficiency and dynamic stability. While numerous studies have explored either substrate temperature or system pressure effects separately, systematic investigations into their coupled effects have not yet been sufficiently explored.

Based on this, the present study systematically investigates the effects of temperature and pressure on bubble nucleation and growth behavior under rapid wall heating conditions with a pressure-control plate.

In this study, molecular dynamics simulations were employed to investigate the nucleation behavior of liquid argon on Pt substrates under rapid wall heating, with constant-pressure conditions maintained by a pressure-control plate. The simulation captured the dynamic processes of bubble nucleation, growth, and vapor film formation under different substrate temperatures and system pressures. We analyzed heat flux variations and temperature distributions, as well as calculating nucleation time and critical nucleation volume. Furthermore, nucleation maps in the temperature−pressure space revealed three characteristic regions: a low-temperature non-nucleation region, an intermediate transition region highly sensitive to pressure, and a high-temperature easier nucleation region. This study on the Ar/Pt system reveals molecular-level bubble nucleation mechanisms and provides insights for predictive modeling of macroscale phase-change behavior.

SIMULATION SYSTEM AND METHOD

Simulation System

In our research, the molecular dynamics method is utilized to investigate the bubble nucleation behavior of an argon film placed on a cavity substrate. Argon and platinum are employed as the working materials. Platinum (Pt), characterized by its high melting point and excellent thermal conductivity, serves as a stable heating substrate. Moreover, the well-established interaction parameters between argon and platinum facilitate modeling of heat transfer across the liquid−solid interface and the associated nucleation phenomena.[55,70]

Figure 1 shows the schematic of the initial system configuration, which is a cuboid simulation box with

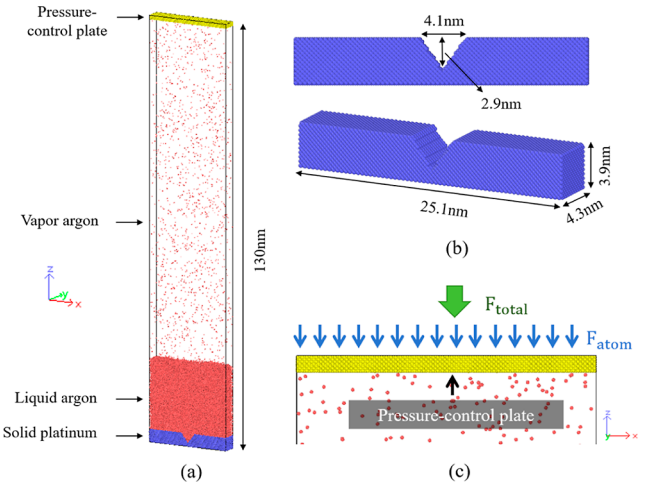

Figure 1. (a) Configuration of the initial simulation system: solid platinum substrate (blue) at the bottom, liquid argon layer (red) in the middle, and Pt pressure-control plate (yellow) at the top; (b) structural configuration and geometric parameters of the solid platinum substrate; (c) schematic illustration of the pressure-control plate mechanism.

dimensions of 25.1 nm (x) × 4.3 nm (y) × 130 nm (z). The shorter length in the y-direction reduces the total number of atoms, thereby decreasing computational cost, and also helps to prevent the formation of multiple bubbles along the y-axis, enabling a focus on the nucleation and growth of individual or a few bubbles. The extended domain size in the z-

https://doi.org/10.1021/acs.langmuir.5c06175
Langmuir 2026, 42, 7212−7227

direction provides sufficient space for the vapor phase, allowing for an adequate number of vapor atoms to better compute pressure, density, and temperature. The system consists of a solid platinum substrate (blue) at the bottom, a liquid argon layer (red) in the middle, and a Pt pressure-control plate (yellow) at the top. At the bottom of the simulation box, 27731 metal platinum atoms are placed in a face-centered cubic lattice (FCC (1 1 1)), and 50000 liquid atoms are arranged on the platinum substrate. The pressure-control plate is composed of 9856 atoms. During the equilibration process, a portion of the liquid argon atoms near the free surface evaporate into the upper region and transition into the gas phase. Periodic boundary conditions[71] are applied in both the *x*- and *y*-directions. In the *z*-direction, a "shrink-wrapped" boundary condition is adopted, which can adjust itself to maintain all particles within the simulation box and provides a mechanism for regulating system pressure during the phase change process.[72]

The Pt substrate has a thickness of 3.9 nm, while the V-groove features a depth of 2.9 nm and a width of 4.1 nm. As shown in Figure 1b, the platinum substrate is divided into three functional regions along the *z* direction. The bottom two layers of Pt atoms are fixed to prevent atomic penetration and structural deformation during heating. The next two layers above are coupled to a Langevin thermostat and serve as the heat source region for energy input into the system. The remaining upper Pt atoms constitute the conductive region, which transfers heat steadily to the overlying liquid argon layer. To achieve controllability and stability of bubble nucleation position, as well as to ensure reproducibility of simulation, this study introduces V-shaped grooves to induce bubble generation.[56,70,73]

Simulation Method

In our molecular dynamics simulations, the interatomic potentials of Ar−Ar, Pt−Pt, and Ar−Pt are calculated by the standard 12-6 Lennard-Jones (L-J) potential function[74] expressed as

$$\Phi(r_{ij}) = 4\varepsilon\left[\left(\frac{\sigma}{r_{ij}}\right)^{12} - \left(\frac{\sigma}{r_{ij}}\right)^{6}\right],\ r_{ij} < r_c \tag{1}$$

where r_{ij} is the distance between two particles, ε is the depth of the potential energy well, and σ is the distance at which the interparticle potential becomes zero, representing the finite size of the particles. Considering the balance between computational accuracy and cost, the cutoff distance r_c is set to 1.2 nm in this study.[75,76]

The Lorentz−Berthelot mixing rule[77] is used to calculate the Lennard-Jones (LJ) potential parameters between Ar and Pt atoms, expressed as

$$\sigma_{Ar-Pt} = \frac{\sigma_{Ar-Ar} + \sigma_{Pt-Pt}}{2} \tag{2}$$

$$\varepsilon_{Ar-Pt} = \sqrt{\varepsilon_{Ar-Ar}\cdot\varepsilon_{Pt-Pt}} \tag{3}$$

The LJ potential parameters between Ar and the Pt atoms in the pressure-control plate were set to relatively extreme values, as listed in Table 1. These parameters were determined based on visualizations to ensure that Ar atoms would immediately rebound upon contacting the pressure-control plate rather than being adsorbed or nucleating on it, thereby clearly distinguishing the plate from the substrate. In the simulations, the substrate served as the actual heat source, and bubble nucleation occurred only near the substrate surface, far below the position of the pressure-control plate. Therefore, these extreme LJ parameters were introduced only to eliminate undesired interactions with the pressure-control plate and do not significantly influence the nucleation behavior or the main simulation results.

Table 1. Lennard-Jones Parameters[70]

interaction type	ε/eV	σ/nm
Ar−Ar	0.0104	0.3405
Pt−Pt	0.5219	0.2475
Ar−$Pt_{substrate}$	0.0737	0.2940
Ar−$Pt_{controlP}$	0.0010	3.5000

Our simulation system uses a strongly hydrophilic Pt substrate with a V-shaped groove—having a contact angle 0°—as determined by the Lennard−Jones interaction parameters between Pt and Ar atoms.[70] Both the groove geometry and the surface wettability play crucial roles in bubble nucleation. As reported in ref 70, strongly hydrophilic groove enables liquid atoms to quickly obtain much kinetic energy to break their potential restriction and convert into a bubble nucleus in a short time. In addition, nanostructured surfaces such as V-shaped grooves facilitate a large heat transfer area, which further accelerates bubble nucleation compared to a smooth substrate.[56] Therefore, both the strong hydrophilicity and the V-shaped nanostructure are expected to exhibit more reproducible nucleation times within simulation time span, leading to statistical stability. More detailed information is provided in the Supporting Information.

In MD simulations with free liquid surfaces, a fixed wall is often used at the top to prevent atom escape, but it restricts volume expansion and causes pressure buildup.[57,59,78] To dynamically control pressure, our study introduces a movable Pt piston-like wall at the top, called the pressure control plate.[27] The wall moves freely along the *z*-axis, driven by the balance between an external force and internal pressure. A total force F_{total} = PA is applied downward on the wall, shown as Figure 1c, where P is the target pressure and A is the area of the pressure-control plate. This total force is uniformly distributed over all Pt atoms in the plate, so that each atom experiences a constant external force of[79]

$$F_{atom} = \frac{F_{total}}{N_{Pt_{controlP}}} = \frac{PA}{N_{Pt_{controlP}}} \tag{4}$$

where $N_{Ptcontrol\ P}$ is the number of atoms in the pressure-control plate.

The simulation consists of three stages: NVT equilibration, NVE equilibration, and heating. The first stage, illustrated in Figure 2a, involves equilibrating the system under the NVT ensemble at 90 K for 27 ns. No external pressure is imposed on the top pressure-control plate during this stage. The equilibrium vapor pressure P_{equil} of the system at 90 K is determined to be approximately 1.54 atm (see Figure 3 for NVT equilibrium stage). In the second stage, the system transitions to the NVE ensemble for 5 ns while maintaining the substrate's heat source layer at 90 K using a Langevin thermostat. The *z*-direction boundary condition is switched to "shrink-wrapped," and a constant target pressure *P* is applied to the pressure-control plate. When $P = P_{equil}$, the wall oscillates near its initial height, and the system snapshot at one moment, as demonstrated in Figure 2b, confirms that the equilibrium

https://doi.org/10.1021/acs.langmuir.5c06175
Langmuir 2026, 42, 7212−7227

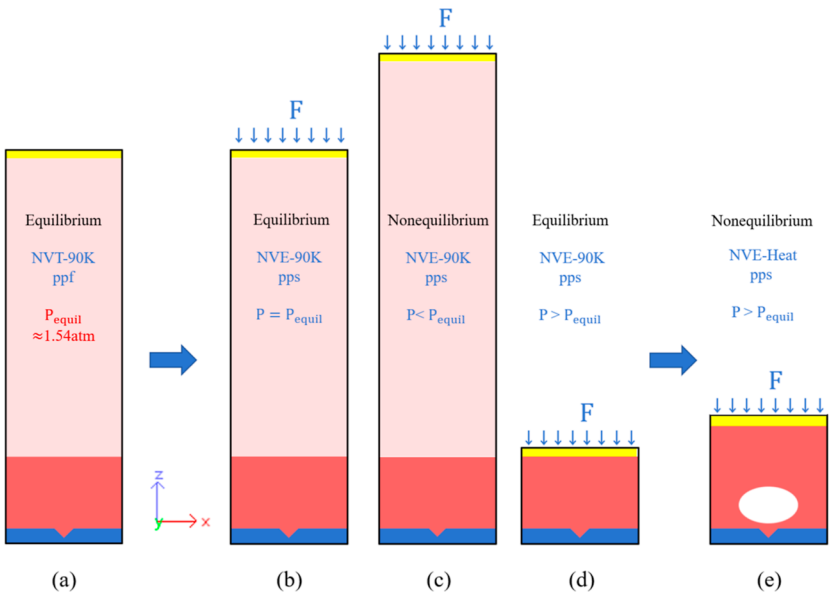

Figure 2. Schematic of our simulation process (a) equilibrated state of the NVT ensemble at 90 K. The pressure-control plate (top) has no applied pressure; P_{equil} denotes the system equilibrium pressure. (b) Equilibrated state of the NVE ensemble at 90 K with the pressure-control plate set to $P = P_{equil}$. (c) NVE ensemble at 90 K when $P < P_{equil}$. (d) Equilibrated state of the NVE ensemble at 90 K with $P > P_{equil}$. (e) Snapshot during the heating stage. Notes: Black text describes system states; blue text indicates simulation settings; red text labels key outcomes. "ppf" denotes periodic boundaries in x and y directions with fixed z-boundary; "pps" represents periodic x and y boundaries with shrink-wrapped z-boundary.

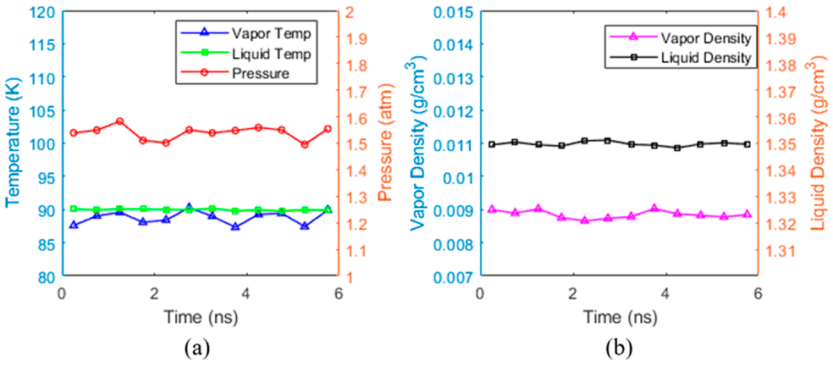

Figure 3. Thermodynamic properties during the final 6 ns of the NVT equilibration stage. (a) Liquid temperature, vapor temperature and system pressure. (b) Liquid density and vapor density.

vapor pressure of the system at 90 K under NVT conditions is around 1.54 atm. If $P < P_{equil}$, illustrated in Figure 2c, the wall ascends continuously due to liquid evaporation and system expansion, rendering stable pressure maintenance impossible. Conversely, when $P > P_{equil}$, shown as Figure 2d, the wall compresses the system downward, suppressing evaporation and enabling stable pressure conditions—a prerequisite for subsequent heating studies. Therefore, to ensure simulation stability and reproducibility in the heating stage, all pressure settings used in this work are above P_{equil}. The final heating stage employs the NVE ensemble up to 15 ns to observe bubble nucleation and growth. The platinum substrate's heat source layer is instantaneously switched from 90 K to the target temperature, while the pressure-control plate maintains the constant value set during NVE equilibration. During heating, once the system pressure exceeds the wall's set pressure, the wall is progressively displaced upward as shown in Figure 2e.

The Velocity-Verlet algorithm[80] is used with a time step of 0.005 ps, and data are recorded every 1000 steps. In this study, all simulation utilize the large-scale atomic/molecular massively parallel simulator (LAMMPS) developed by Plimpton,[25] and atom trajectories are visualized using OVITO,[26] an open-source visualization tool developed by Stukowski at Sandia National Laboratory.

CALIBRATION

Calibration of Equilibrium State

To verify that the system has reached equilibrium, the thermodynamic properties during the final 6 ns of the NVT equilibration stage were analyzed, as shown in Figure 3a, which presents the liquid temperature, vapor temperature, and system pressure. Both the liquid and vapor phases reached thermal equilibrium at approximately 90 K, with the liquid temperature exhibiting smaller fluctuations. The system pressure stabilized at 1.54 (±0.025) atm, in agreement with the equilibrium vapor pressure of argon 1.41 (±0.167) at 90 K reported in the literature.[81] Figure 3b shows the corresponding densities of the liquid and vapor phases. The average liquid density is 1.349 (±0.00082) g/cm^3, which is close to the reference value of 1.379 g/cm^3 from the NIST database. The vapor density is

https://doi.org/10.1021/acs.langmuir.5c06175
Langmuir 2026, 42, 7212−7227

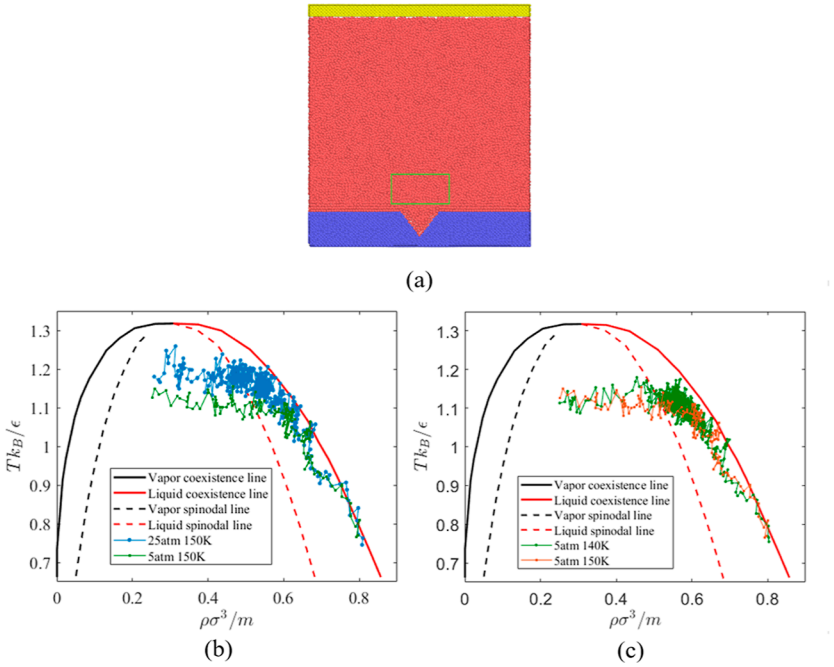

Figure 4. (a) The nucleation region defined by the green rectangular box (x = 9−16 nm, y = 0−4.3 nm, z = 4.5−8 nm); Thermodynamic evolution trajectories of system (b) substrate temperature fixed at 150 K with system pressures of 25 and 5 atm; (c) system pressure fixed at p = 5 atm with substrate temperatures of = 140 and 150 K. The temperature (Tk_B/ε) and averaged density ($\rho\sigma^3$/m) of argon are plotted on the phase diagram, where m is the atom mass of argon.[85]

0.0088 (±0.00012) g/cm^3, which also agrees reasonably well with the NIST value of 0.0074 g/cm^3.[82]

Calibration of Phase Diagram of Nucleation

To determine whether bubble nucleation occurs in the simulated system, this study employs a phase diagram based on the equation of state proposed by Nicolas et al.[83] This phase diagram, consisting of the coexistence curve and the spinodal line, serves as a critical criterion for assessing bubble nucleation conditions.[84−86] The coexistence curve represents the relationship between fluid density and temperature at the equilibrium liquid−vapor state, while the spinodal curve represents the limit of thermodynamic stability, and the metastable region is bounded between the coexistence curve and the spinodal curve.[86] Since bubble nucleation is a phase change process from liquid to vapor, the liquid spinodal line and coexistence curve are sufficient to characterize the physical process of bubble nucleation.[86] Initially, the state point is near the saturated liquid line, showing argon atoms. As heating continues, density decreases and temperature rises, moving the state point to the metastable region. When it enters the spinodal line region, bubble nucleation starts.[33]

In this work, the nucleation region is defined as the space around the largest bubble nucleus, as shown in green rectangle in Figure 4a, where the liquid film is analyzed while avoiding interference from the adsorbed argon layer near the substrate. Simulations indicate that the liquid density within the nucleation region gradually decreases with increasing temperature. By monitoring the relationship between this density variation and the phase diagram, the conditions for bubble nucleation can be effectively determined. Sampling is performed every 2000 timesteps to compute the temperature of argon (Tk_B/ε) and averaged density ($\rho\sigma^3$/m), which are then plotted on the phase diagram to evaluate the thermodynamic state, where m is the atom mass of argon.[85]

Figure 4b,c illustrates the distribution of thermodynamic state points of four systems. It is observed that as the temperature of liquid argon increases, the state points progressively approach and eventually cross into the spinodal region, confirming that the liquid film meets the thermodynamic conditions for bubble nucleation.[87−89] The system state is recorded every 2000 timesteps; therefore, the local density of trajectory points reflects how long the system remains near a given thermodynamic state. In Figure 4b, under the same substrate temperature, the trajectory at 25 atm exhibits a higher point density in the metastable liquid region than that at 5 atm. Similarly, in Figure 4c, under the same system pressure, the 140 K trajectory shows a higher point density in the metastable liquid region than that at 150 K. This indicates that, under higher pressure or lower temperature, the system stays in the metastable state for a longer time, which also implies a longer time required to trigger nucleation. A more detailed discussion of this part is provided in the Supporting Information.

RESULTS AND DISCUSSION

Bubble Nucleation and Growth Behavior

The heating process can be divided into three phases. In the first phase, the substrate temperature is instantaneously raised from 90 K to the target temperature, causing the argon liquid to heat up and exhibit a decrease in density. However, no stable bubbles are formed at this point. The second phase corresponds to bubble nucleation and growth. As the bubbles continue to grow and expand to cover the substrate surface, the substrate gradually becomes replaced by a gas layer, leading to the third phase, the film boiling regime, in which the liquid is separated from the substrate by a gaseous film. Taking a simulation at a system pressure of 5 atm and a substrate

https://doi.org/10.1021/acs.langmuir.5c06175
Langmuir 2026, 42, 7212−7227

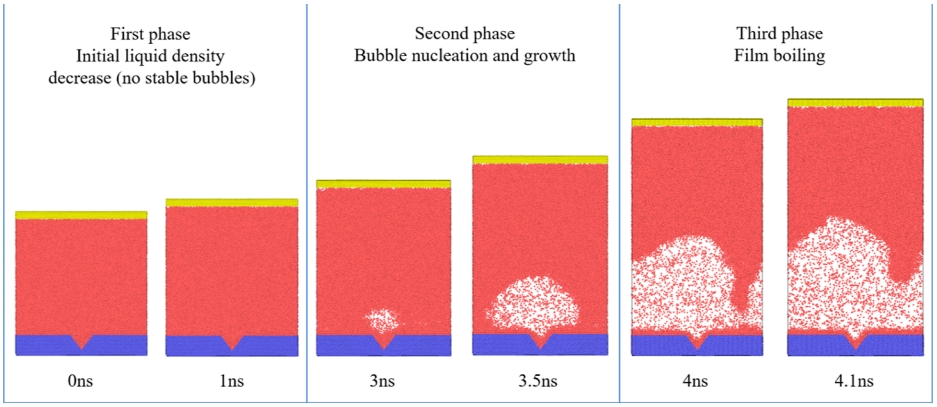

Figure 5. Front-view snapshots of the heating process in the $x-z$ plane at a pressure of 5 atm and a substrate temperature of 145 K.

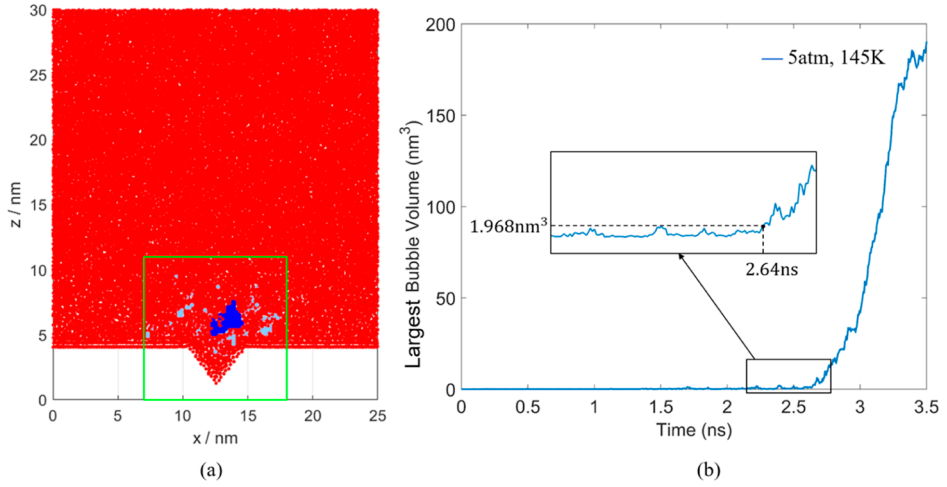

Figure 6. (a) Green rectangle (7−18 nm, y = 0−4.3 nm, z = 0−11 nm) defines the bubble tracking region. Red dots are Ar atoms, blue dots the largest bubble, and light-blue dots smaller bubbles. (b) Temporal evolution of the largest bubble volume within this region. The moment the bubble volume first exceeds the critical nucleation volume is taken as the nucleation time.

temperature of 145 K as an example, the heating process is illustrated in Figure 5.

The focus of this study is on the bubble nucleation and growth phase. A nucleation event is defined as follows: during the simulation, when the volume of a cavity first exceeds the critical nucleation volume and continues to grow thereafter, it is identified as a nucleation event. The time at which nucleation occurs is defined as the nucleation time, with the corresponding volume taken as the critical nucleation volume.

To calculate bubble volumes, we employed a cavity identification method based on a three-dimensional grid and local atomic density.[85,88] Specifically, the liquid region is divided into uniform cubic grid cells with dimensions of 0.2 nm × 0.2 nm × 0.2 nm. For each grid cell center, a neighborhood search radius of $1.2\sigma_{Ar}$ is defined to check for the presence of argon atoms and σ_{Ar} equals 0.34 nm; if no atoms are detected within this range, the cell is marked as a cavity point. All contiguous cavity cells are then grouped to form a bubble.

The snapshot at 3 ns in Figure 5 shows that the nucleation site is approximately located above a V-shaped groove, where the bubble nucleus has stabilized and entered the growth phase. A bubble tracking region was defined for the calculation of bubble volume. To ensure complete coverage of the bubble during nucleation, this region was specified as x = 7−18 nm, y = 0−4.3 nm, and z = 0−11 nm, corresponding to the green box shown in Figure 6a. Although bubbles predominantly nucleate near the groove within the liquid phase,[89] a small number also forms at other locations on the substrate. Therefore, the position of the bubble tracking region is adjusted according to the actual nucleation site.

After defining the bubble tracking region, we tracked the evolution of the largest bubble volume within this region to determine the critical nucleation volume and nucleation time, which is illustrated in Figure 6b. The critical nucleation volume[26] is defined as the minimum volume required for a bubble to exist stably and continues to grow and to evolve into a larger bubble rather than to collapse. Cavities smaller than this volume tend to collapse due to their inability to overcome the nucleation barrier, while those exceeding it grow rapidly. In this study, the critical nucleation volume is operationally recognized as the maximum bubble volume reached just before the bubble enters the continuous growth stage, around the 2.64 ns in the case of Figure 6a; the volume in the continuous growth stage is always larger than this value. The moment when the bubble volume first surpasses this value is taken as the nucleation time. As shown in Figure 6b, the evolution curve of the largest bubble volume within the bubble tracking region indicates a critical nucleation volume of 1.968 nm^3.

Nagayama et al.[90] and Zhao et al.[71] have shown that, on hydrophilic substrates, bubble nucleation occurs within the superheated liquid close to the substrate, rather than directly at

https://doi.org/10.1021/acs.langmuir.5c06175
Langmuir 2026, 42, 7212−7227

the interface, and thus can be regarded as homogeneous nucleation. Consistently, as shown in Figure 6a, the nucleation sites in the present study are located within the bulk liquid rather than at the solid surface, which satisfies the definition of homogeneous nucleation.[91,92]

Heat Flux During Heating Stage

In this study, to quantify the heat transfer rate from the substrate to the argon system, the heat flux was analyzed based on the principle of energy conservation. The liquid argon and the pressure-control plate are treated as a single system. The rate of change of the total energy of this system, q_{all}, is equal to the sum of the heat flux supplied by the substrate, q_{heat}, and the work done the pressure-control plate, q_W. The heat flux from the substrate to the liquid argon system then can be calculated as $q_{heat} = q_{all}$-q_W.

The power associated with the work done by the plate is given by $q_W = P\Delta h/\Delta t$, where h denotes the average height of the pressure-control plate particles. Taking the system at a pressure of 5 atm and a substrate temperature of 145 K as an example, the temporal evolution of the heat flux q_{heat} is shown in Figure 7. The original heat flux curve was smoothed using

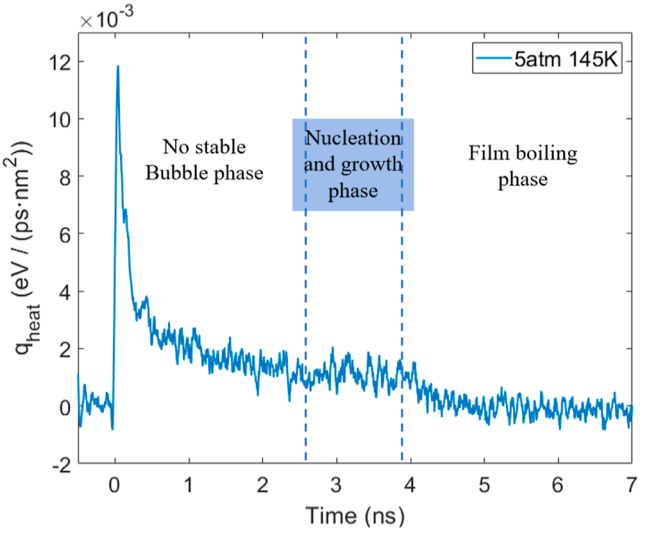

Figure 7. Evolution of the heat flux from the substrate to the liquid argon during the heating process under a system pressure of 5 atm and a substrate temperature of 145 K.

the Savitzky−Golay filter,[93] which is commonly employed in signal processing. Within each window containing 21 adjacent data points, corresponding to a total temporal span of 0.105 ns, the filter fits a third-order polynomial and replaces the center point with the fitted value, effectively reducing noise while preserving the overall trend.

During the heating stage, the substrate temperature is suddenly increased to 145 K at time zero. Due to the large temperature difference between the substrate and the liquid argon, the heat flux from the substrate to the liquid rises sharply and reaches a peak. The heat is first transferred to the thin layer of liquid molecules adjacent to the substrate, causing a rapid temperature increase in this layer and a significant reduction in the interfacial temperature difference. Since the heat flux mainly depends on the interfacial temperature difference rather than the temperature of the higher up liquid, it decreases rapidly afterward, with the rate of decline gradually slowing. As bubbles form and grow above the substrate, the thermal resistance of the gas leads to pronounced fluctuations and further reduction in the heat flux. The heat flux reaches its lowest levels once the vapor film completely covers the substrate surface. The starting time of the third stage is partially dependent on the width of the system, not having physical meaning, which is also why we do not pay more attention to the third stage.

Effect of Operating Conditions on Bubble Nucleation Behavior

To systematically investigate the effects of substrate heating temperature and system pressure on nucleation and growth behavior, two sets of simulations were designed. In the first set, the system pressure was fixed at 5 atm, and substrate temperatures of 140, 143, 145, 150, and 155 K were considered. In the second set, the substrate temperature was fixed at 150 K, and system pressures of 5, 10, 15, 20, and 25 atm were considered. The rationale for selecting these specific substrate temperatures is provided in the Supporting Information.

To determine the required number of repeated simulations, the statistical stability of nucleation time was examined. The results indicate that averaging over two and three repeated simulations yields an approximate 2.3% difference in the mean nucleation time, suggesting that at least three repeated simulations are necessary to obtain statistically reliable nucleation times, same as previous studies.[56,85,94] Increasing the number of repetitions improves statistical convergence: with three to four repetitions, the difference in mean nucleation time is around 1.9%, and with four to five repetitions it further decreases to below 0.67%. To ensure sufficient stability and reproducibility while minimizing the influence of random fluctuations on the determination of nucleation times, five repeated simulations were conducted for each condition in this study.

Effect of Substrate Temperature on Bubble Nucleation Behavior. Under a constant system pressure of 5 atm, a series of molecular dynamics simulations performed by varying the substrate temperature from 140 to 155 K, and one simulation for each condition was selected for analysis. The evolution snapshots of three representative cases are shown in Figure 8. It can be seen that increasing the substrate temperature significantly advances the onset of bubble nucleation. At 140 K, the nucleation time is approximately 6.65 ns, whereas at 150 K it is reduced to about 1.06 ns. Moreover, at elevated temperatures, bubbles not only form earlier but also expand to cover the substrate more rapidly. We note that Figure 8a shows evaporated gas above the liquid film. The saturation vapor pressure of argon is 5.0 atm at 106 K;[95] thus, when the local temperature exceeds this value under a system pressure of 5 atm, evaporation and a detectable vapor region are favored, whereas vapor formation is suppressed below this threshold. At the nucleation moment for the 140 K case (Figure 8a, 6.65 ns), the temperature in the upper part of the liquid film (outside the vapor region) has already surpassed 106 K (Figure 11), so the local saturation vapor pressure exceeds 5 atm, enabling the formation of a stable vapor region above the liquid film.

The simulation results show that, under a fixed system pressure of 5 atm, as the substrate temperature increases from 140 to 155 K, the nucleation time decreases from 6.30 to 0.48 ns, and the critical nucleation volume decreases from 2.67 nm^3 to 0.70 nm^3, as presented in Figure 9.

https://doi.org/10.1021/acs.langmuir.5c06175
Langmuir 2026, 42, 7212−7227

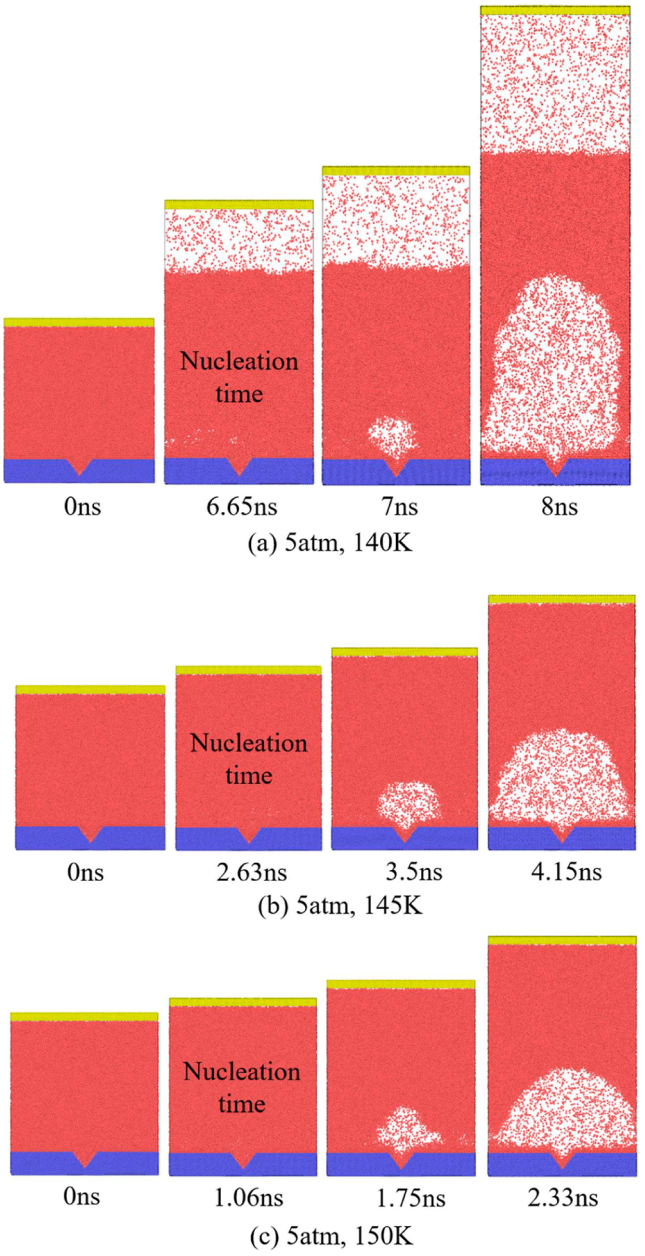

Figure 8. Snapshots of simulation results under a system pressure of 5 atm at different substrate temperatures: (a) 140 K, (b) 145 K and (c) 150 K.

During the initial heating stage, a higher substrate temperature induces a stronger instantaneous heat flux from the substrate to the liquid argon, as illustrated in Figure 10a, which promotes more rapid energy transfer into the liquid. As further shown in Figure 10b, the solid−liquid interface has a relatively low Kapitza thermal resistance at the early stage of heating, and thus facilitating efficient heat transfer across the interface. However, the stronger instantaneous heat flux accelerates the development of local superheating and low-density regions near the interface, which in turn leads to an increase in the interfacial thermal resistance at later times. This effect is further illustrated by the corresponding temperature fields in Figure 11. For instance, for "5 atm, 150 K" case, the liquid adjacent to the substrate reaches a higher local temperature with a steeper system temperature gradient in shorter time (1.06 ns), compared with the "5 atm, 140 K" case in 6.65 ns. Consequently, liquid in "5 atm, 150 K" case attains the superheating required to overcome the nucleation barrier more quickly, thereby initiating nucleation in a smaller nucleation time, as illustrated in Figure 9a.

To elucidate the mechanism of bubble formation on grooved substrates, Chen et al.[70] proposed the "PK" criterion, in which the liquid atoms possess two types of energy: the potential energy, associated with the local density distribution, restricts atomic motion, while the kinetic energy, determined by temperature, reflects the ability of atoms to move freely. Bubble nucleation occurs when a group of atoms obtains sufficient kinetic energy to overcome the local potential energy. From a kinetic perspective, increasing the substrate temperature enhances the thermal motion of liquid molecules, providing them with higher kinetic energy to overcome potential energy and disrupt local structural stability. As a result, even smaller vapor cavities can remain stable, leading to a decrease in the critical nucleation volume, as illustrated in Figure 9b.

Effect of System Pressure on Bubble Nucleation Behavior

Under a constant system pressure of 5 atm, simulations were conducted at different substrate temperatures, and for each condition, a single independent simulation was randomly selected at various time points for comparative analysis. The evolution snapshots of three representative cases are shown in Figure 12.

The simulation results show that, under a fixed substrate temperature of 150 K, as the system pressure increases from 5 to 25 atm, the nucleation time is prolonged from 1.12 to 4.04 ns, and the critical nucleation volume increases from 1.16 nm^3 to 3.45 nm^3, as presented in Figure 13.

This trend can be interpreted from the perspective of the energy distribution of the liquid and the mechanism of bubble formation. Since the substrate temperature is uniformly 150 K, the heat flux shows little variation under different pressures. As shown in Figure 14a, the heat flux of the liquid rapidly increases and reaches a peak during the early heating stage. The enlarged view of the peaks indicates that their magnitudes shows no significant differences. Similarly, Figure 14b shows that the initial growth rate of the Kapitza thermal resistance after the heat-flux peak also exhibits no significant difference under various pressures. As illustrated in Figure 15, the temperature distributions at 0.75 ns are nearly identical under various pressures, further confirming that the heat transfer rates of the systems are similar.

As the system pressure increases, the liquid density rises and the intermolecular spacing decreases, making bubble formation more difficult. Bubble nucleation thus requires a higher local superheating to overcome the nucleation barrier. Since the heat flux from the substrate to the liquid remains almost the same under different pressures, the liquid at higher pressure needs a longer time to accumulate sufficient kinetic energy, resulting in a delayed nucleation, as shown in Figure 13a. This observation is in agreement with the trend found by Qiu et al.[20]

The prolonged nucleation time allows the liquid to absorb more heat, increasing the kinetic energy and facilitating the overcoming of the nucleation barrier. Meanwhile, as shown in Figure 15, the liquid expands slightly and its density decreases as the temperature rises, which promotes the expansion and stabilization of the bubble nucleus. Consequently, larger

https://doi.org/10.1021/acs.langmuir.5c06175
Langmuir 2026, 42, 7212−7227

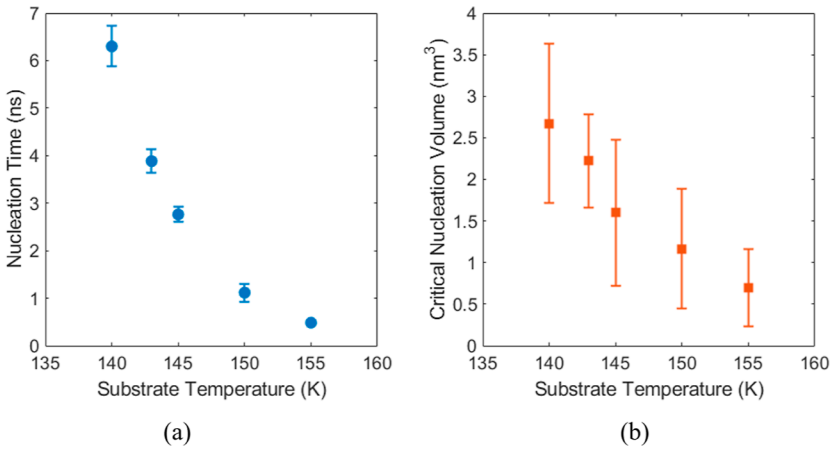

Figure 9. (a) Variation of nucleation time with substrate temperature; (b) variation of critical nucleation volume with substrate temperature.

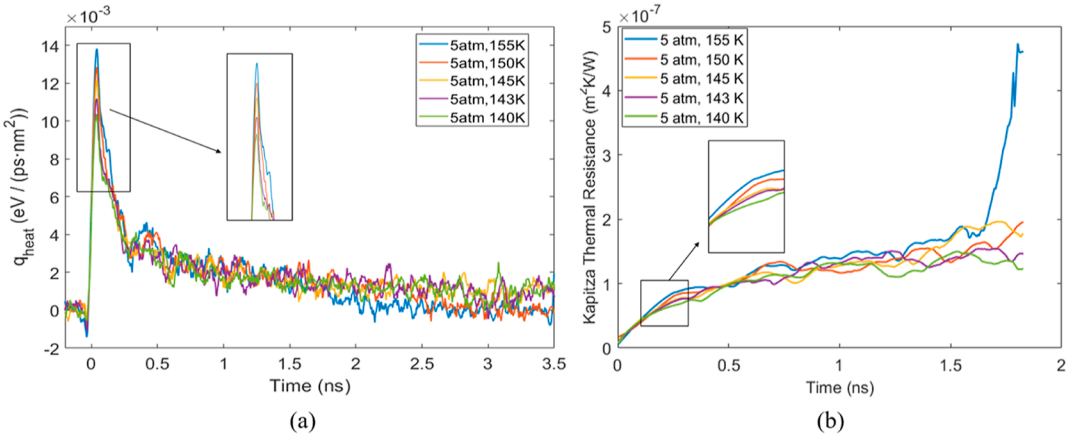

Figure 10. Temporal evolution of the (a) q_{heat} from the substrate to liquid argon and (b) Kapitza thermal resistance under a system pressure of 5 atm at different substrate temperatures.

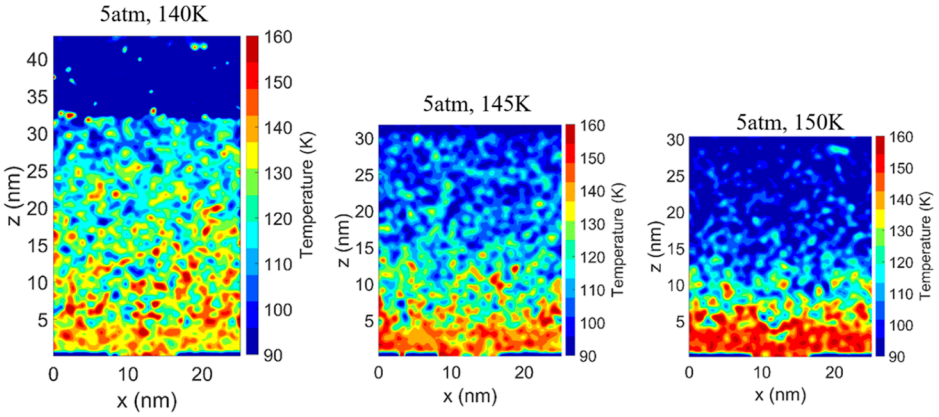

Figure 11. Temperature distribution in the $x-z$ plane under a system pressure of 5 atm at different substrate temperatures at the nucleation time. The nucleation times corresponding to 5 atm at 140, 145, and 150 K are 6.65, 2.63, and 1.06 ns, respectively. The z-range of each plot corresponds to the total height of the system at the corresponding time, which increases as the pressure-control plate moves upward during heating.

bubbles are formed at the nucleation moment under high-pressure conditions, as shown in Figure 13b.

Nucleation Behavior under Varying Substrate Temperature and System Pressure

Based on the analyses in the previous sections, this section extends the study to capture the coupled effects of system pressure and substrate temperature by constructing nucleation maps in the two-dimensional parameter space. Considering the limitations of available computational resources and simulation time, the heating simulations in this study were limited to a run time of 17.5 ns.

As shown in Figure 16, the nucleation time exhibits pronounced dependencies on both temperature and pressure. To quantitatively compare the relative influence of system pressure and substrate temperature on the onset of nucleation, a direct numerical comparison of the variation in nucleation

https://doi.org/10.1021/acs.langmuir.5c06175
Langmuir 2026, 42, 7212−7227

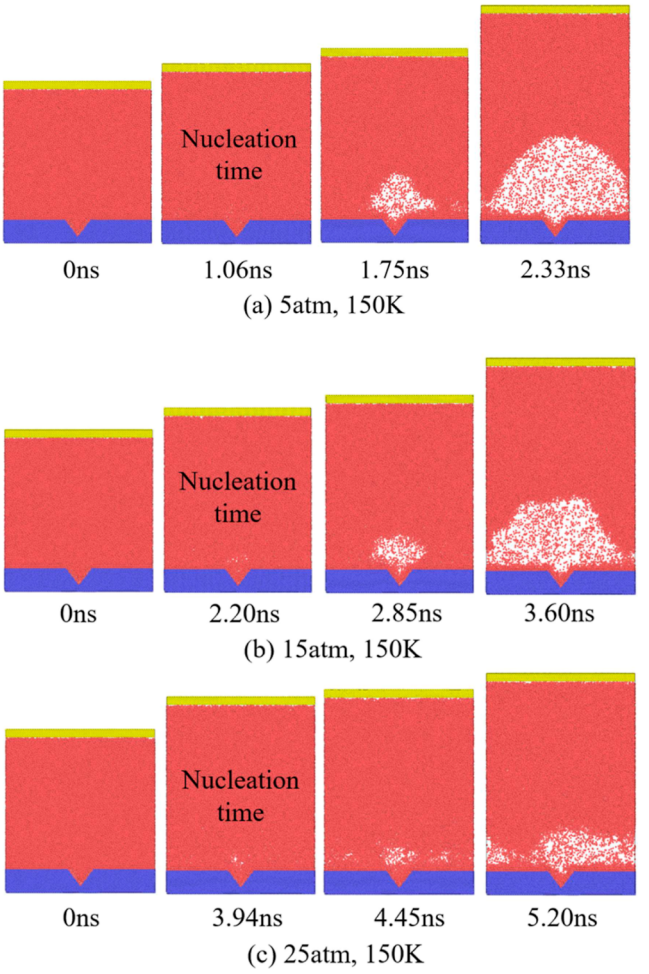

Figure 12. Snapshots of simulation results under a substrate temperature of 150 K at different system pressures: (a) 5 atm, (b) 15 atm and (c) 25 atm.

time was performed. At 2 atm, when the substrate temperature increases from 138 to 150 K, the nucleation time decreases from 7.61 to 1.05 ns, a reduction of approximately 86%; similarly, at 10 atm, the same temperature increase reduces the nucleation time from 10.21 to 1.64 ns, corresponding to a decrease of about 84%. In contrast, at a fixed temperature of 143 K, decreasing the pressure from 25 to 2 atm reduces the nucleation time from 12.68 to 2.71 ns, a reduction of approximately 79%. Within the unit system adopted in this work, the nucleation time is therefore slightly more sensitive to temperature than to system pressure. It is noteworthy that in the lower temperature range (130−135 K), no nucleation occurs regardless of pressure, indicating the existence of a nucleation threshold. Moreover, at higher pressures (≥25 atm), "no nucleation" events are observed even at elevated temperatures, reflecting the suppressive effect of high pressure on the nucleation process.

The boundary between nucleated and non-nucleated regions was fitted using a quadratic polynomial, yielding the following expression

$$P = -0.284T^2 + 82.9T - 6017.3 (136.5K \leq T \leq 144K) \quad (4)$$

with a coefficient of determination $R^2 = 0.929$. Here, T (K) denotes the substrate temperature and P (atm) represents the system pressure. The fitted curve is shown as a black dashed line in Figures 16 and in 17, which can be used to approximately distinguish between the nucleation and non-nucleation regions.

As shown in Figure 17, the critical nucleation volume is also significantly influenced by both temperature and pressure. At a given pressure, the critical nucleation volume decreases with increasing instantaneous heating temperature. For instance, at 2 atm, the volume decreases from 2.60 nm^3 at 138 K to 0.99 nm^3 at 150 K; at 10 atm, it decreases from 3.32 nm^3 at 138 K to 1.87 nm^3 at 150 K. This indicates that, under higher temperature conditions, smaller bubble volumes are sufficient to meet the critical nucleation criteria, thereby facilitating nucleation.

Meanwhile, at a fixed temperature, the critical nucleation volume increases markedly with increasing pressure. For example, at 143 K, the critical volume is 1.62 nm^3 at 2 atm and increases to 6.91 nm^3 at 25 atm, suggesting that higher pressure raises the critical bubble volume required for nucleation, thus inhibiting the nucleation process. Notably, at relatively low temperatures (130−135 K), nucleation does not occur under any of the examined pressures, indicating that the critical volume cannot be effectively reached in this temperature range. Furthermore, at high pressures (≥25 atm), the critical nucleation volume remains comparatively large even at elevated temperatures; for example, it reaches 5.41 nm^3 at 25

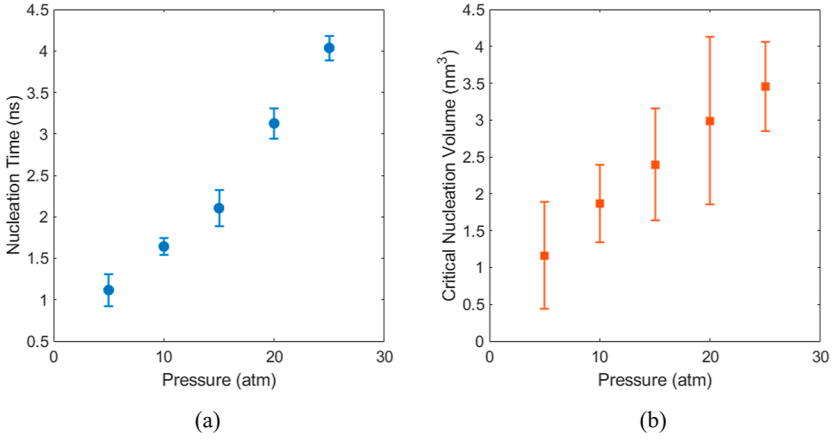

Figure 13. (a) Variation of nucleation time with system pressure; (b) variation of critical nucleation volume with system pressure.

https://doi.org/10.1021/acs.langmuir.5c06175
Langmuir 2026, 42, 7212−7227

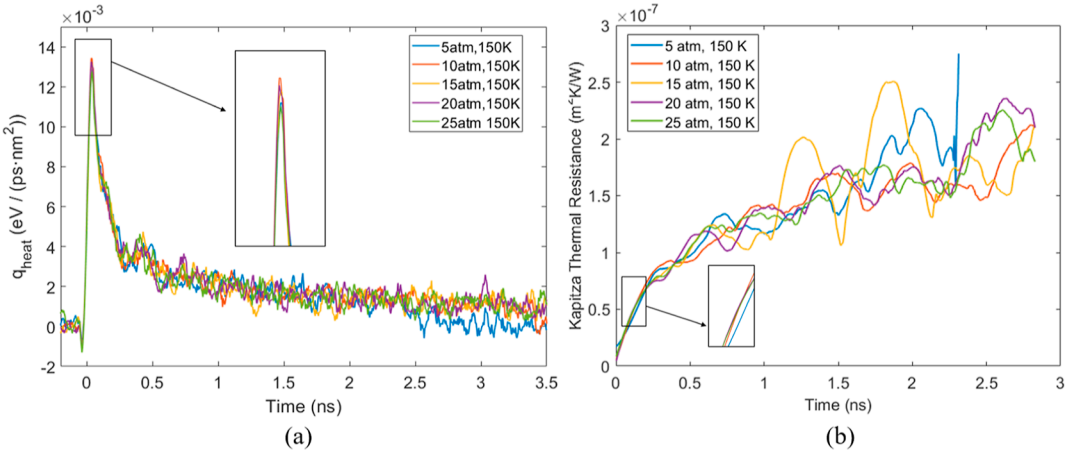

Figure 14. Temporal evolution of the (a) q_{heat} from the substrate to liquid argon and (b) Kapitza thermal resistance under different system pressures, with the substrate temperature set at 150 K.

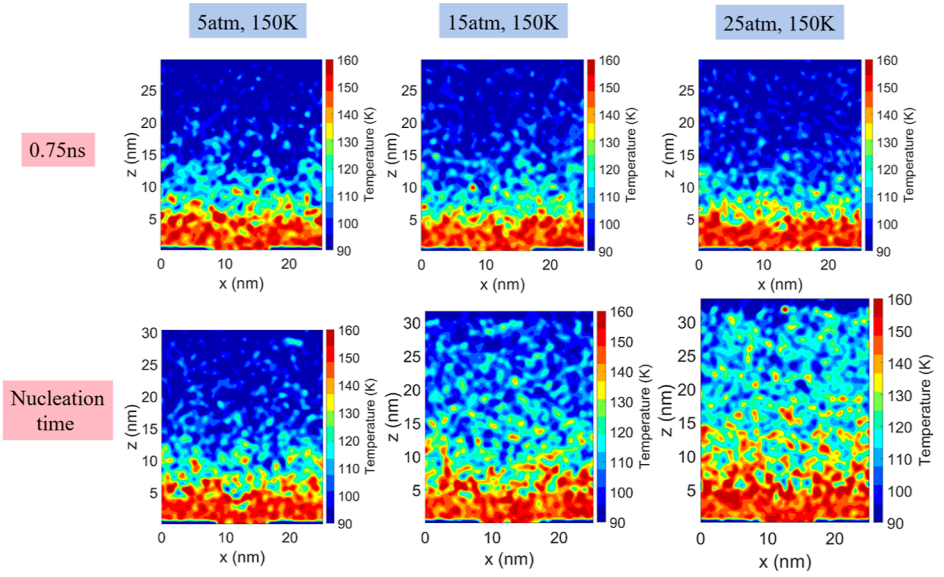

Figure 15. Temperature distribution in the $x-z$ plane under different system pressures, with the substrate temperature fixed at 150 K. Each column corresponds to the same case at different times: the first row shows the temperature distribution at 0.75 ns, and the second row shows the distribution at the corresponding nucleation time. The nucleation times for 150 K at 5, 15, and 25 atm are 1.06, 2.20, and 3.94 ns, respectively. The z-range of each plot corresponds to the total height of the system at the corresponding time, which increases as the pressure-control plate moves upward during heating.

atm and 145 K, and further increases to 8.87 nm^3 at 30 atm and 145 K. This trend further reveals the adverse effect of high pressure on the nucleation process: a higher pressure compels the system to attain a larger critical bubble volume for nucleation to occur, thereby significantly inhibiting the process.

Comparison with existing molecular dynamics studies shows that the bubble nucleation times and critical nucleation scales obtained in this work are in good agreement with literature results in terms of order of magnitude. Previous studies have reported characteristic nucleation times on the order of approximately 1−6 ns,[33,96] and the critical nucleation radius reported in the literature[99] is about 2 nm, corresponding to a critical nucleation volume of 1−10 nm^3. Although differences exist in heating protocols, pressure-control methods, surface wettability, and system size among these studies, the values are in good agreement, in terms of order of magnitude, with the results of our simulations.

Specifically, the system's nucleation behavior in the parameter space investigated can be divided into three regions: a "non-nucleation region" at low temperatures, a "transition region" at intermediate temperatures that is highly sensitive to pressure, and a "strong nucleation region" at high temperatures. In the low-temperature non-nucleation region (130−135 K), no nucleation occurs at any pressure, showing that the thermal driving force is insufficient to overcome the formation barrier. At 138−143 K, the system enters a transition region, where nucleation strongly depends on pressure. At 145−150 K, the strong nucleation region, nucleation occurs at all pressures with short nucleation times and small critical volumes, indicating rapid and stable bubble growth.

CONCLUSIONS

Based on molecular dynamics simulations, this work systematically investigates the bubble nucleation behavior of liquid argon under instantaneous heating of a platinum substrate,

https://doi.org/10.1021/acs.langmuir.5c06175
Langmuir 2026, 42, 7212−7227

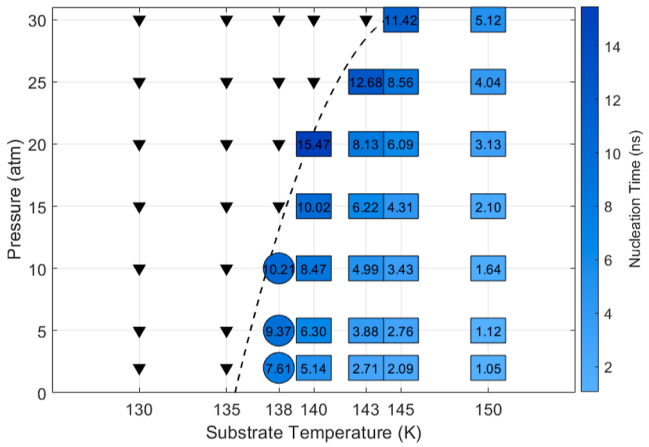

Figure 16. Nucleation time map for up to 17.5 ns. Blue squares indicate that all five independent simulations for a given condition resulted in nucleation, blue circles indicate that only some simulations nucleated, and black triangles indicate that none of the simulations nucleated. The blue symbols represent the nucleation times in nanosecond obtained from simulations under the corresponding substrate temperature and system pressure conditions. Black dashed line is the fitting curve used to approximately distinguish between the nucleation and non-nucleation regions.

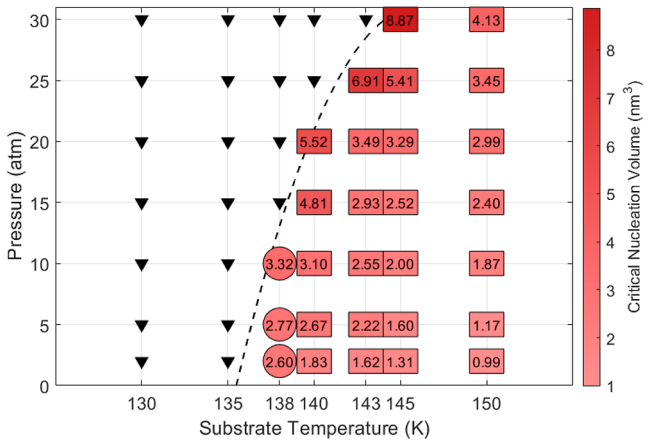

Figure 17. Critical nucleation volume map. Red squares indicate that all five independent simulations for a given condition resulted in nucleation, red circles indicate that only some simulations nucleated, and black triangles indicate that none of the simulations nucleated. The data in the red symbols represent the critical nucleation volume obtained from simulations under the corresponding substrate temperature and system pressure conditions. Black dashed line is the fitting curve used to approximately distinguish between the nucleation and non-nucleation regions.

with particular emphasis on the pressure-control strategy, the coupled effects of temperature and pressure, and the resulting nucleation regimes.

First, a simulation framework incorporating a movable pressure-control plate is developed, enabling effective regulation of the system pressure during nonequilibrium heating. This approach avoids the artificial pressure accumulation commonly encountered in fixed-wall configurations due to volume constraints, and provides a stable computational platform for investigating nucleation under well-controlled pressure conditions.

Second, a cavity identification method combining three-dimensional spatial gridding with local atomic density analysis is employed to determine the nucleation time and the critical nucleation volume. The coupled influence of temperature and pressure on nucleation dynamics is systematically analyzed. At a fixed system pressure of 5 atm, increasing the substrate temperature from 140 to 155 K reduces the nucleation time from 6.30 to 0.48 ns, while the critical nucleation volume decreases from 2.67 nm^3 to 0.70 nm^3. Conversely, at a fixed substrate temperature of 150 K, increasing the system pressure from 5 to 25 atm extends the nucleation time from 1.12 to 4.04 ns and increases the critical nucleation volume from 1.16 nm^3 to 3.45 nm^3. Heat-flux analysis further indicates that although pressure has a limited influence on the instantaneous peak heat flux, it strongly affects the energy accumulation process required for the liquid to reach the local superheated state necessary for nucleation.

Within the substrate temperature range of 130−150 K and the system pressure range of 2−30 atm, temperature−pressure maps of nucleation time and critical nucleation volume are constructed. A predictive boundary function separating nucleation and non-nucleation regimes is obtained, thereby forming a quantitative framework for predicting nucleation behavior. Accordingly, the nucleation process can be classified into three distinct regimes: a low-temperature non-nucleation regime (130−135 K), an intermediate transition regime with strong pressure sensitivity (138−143 K), and a high-temperature strong-nucleation regime (145−150 K).

These results elucidate the coupled roles of temperature and pressure in governing bubble nucleation under instantaneous heating at the molecular scale, and provide a predictive framework for describing nanoscale phase-change processes. Future work will further investigate the influence of different groove geometries and substrate wettability on nucleation modes (homogeneous versus heterogeneous), as well as the influence of uniformly wetting and mixed-wettability surfaces on nucleation sites, nucleation time, and critical nucleation volume. The applicability of classical nucleation theory under nonequilibrium heating conditions will also be systematically assessed.

■ ASSOCIATED CONTENT

Supporting Information

A Supporting Information file (PDF) is available and includes. The Supporting Information is available free of charge at https://pubs.acs.org/doi/10.1021/acs.langmuir.5c06175.

V-shaped groove with a depth of 2.9 nm and a width of 4.1 nm selected for this study. The reason for employing the NVE ensemble following initial NVT equilibration. Evaluation of the influence of the pressure-control plate thickness on the system. Pressure monitoring method. The reason for choosing a hydrophilic V-shaped groove. The rationale for selecting the substrate temperatures. Comparison with existing molecular dynamics studies. The contact angle matching hydrophilicity conditions for substrate and liquid. Ensemble size uncertainty. Choice of simulation box size. Rationality of the heating time window (PDF)

■ AUTHOR INFORMATION

Corresponding Authors

Ziqi Cai − *State Key Laboratory of Chemical Resource Engineering, School of Chemical Engineering, Beijing University of Chemical Technology, Beijing 100029, China;*

https://doi.org/10.1021/acs.langmuir.5c06175
Langmuir 2026, 42, 7212−7227

School of Chemical Engineering, Beijing University of Chemical Technology, Beijing 100029, China;
Email: caiziqi@buct.edu.cn

Zhengming Gao − *State Key Laboratory of Chemical Resource Engineering, School of Chemical Engineering, Beijing University of Chemical Technology, Beijing 100029, China; School of Chemical Engineering, Beijing University of Chemical Technology, Beijing 100029, China;*
Email: gaozm@buct.edu.cn

Authors

Ziqi Li − *State Key Laboratory of Chemical Resource Engineering, School of Chemical Engineering, Beijing University of Chemical Technology, Beijing 100029, China; School of Chemical Engineering, Beijing University of Chemical Technology, Beijing 100029, China;* orcid.org/0009-0005-4227-7037

Jacobus Johannes Derksen − *School of Engineering, University of Aberdeen, Aberdeen AB24 3UE, U.K.;* orcid.org/0000-0002-9813-356X

Complete contact information is available at:
https://pubs.acs.org/10.1021/acs.langmuir.5c06175

Notes

The authors declare no competing financial interest.

■ ACKNOWLEDGMENTS

The authors gratefully acknowledge the financial support from the National Natural Science Foundation of China (No. 22078008).

■ REFERENCES

(1) Dhir, V. K. Boiling Heat Transfer. *Annu. Rev. Fluid Mech.* **1998**, *30*, 365−401.
(2) Liang, G.; Mudawar, I. Review of Spray Cooling − Part 1: Single-Phase and Nucleate Boiling Regimes, and Critical Heat Flux. *Int. J. Heat Mass Transfer* **2017**, *115*, 1174−1205.
(3) Cui, Y.; Guo, F.; Ding, Q.; Cheng, B. Investigation of Cavitation Damage Patterns in Centrifugal Pump Blades under Rotating Flow Fields. *J. Pipeline Sci. Eng.* **2026**, *6*, 100288.
(4) Qu, T.; Luo, J.; Xu, W.; Li, J.; Fu, G.; Ma, Y.; Zhao, Z. Experimental Study on the Collapse Behavior of Cavitation Bubbles under Low Ambient Pressure Conditions. *Ultrason. Sonochem.* **2025**, *114*, 107255.
(5) Yang, J.; Jiang, T.; Liu, B.; Zhang, C.; Zeng, X.; He, L.; Gong, W. Experimental and Numerical Analysis of Bubble Nucleation in Foaming Polymer. *Mater. Des.* **2021**, *203*, 109577.
(6) Han, J. H.; Han, C. D. Bubble Nucleation in Polymeric Liquids. I. Bubble Nucleation in Concentrated Polymer Solutions. *J. Polym. Sci., Part B: Polym. Phys.* **1990**, *28*, 711−741.
(7) Bunyatova, U.; Dogan, M.; Tekin, E.; Ferhanoğlu, O. Ultra-Stable Nano-Micro Bubbles in a Biocompatible Medium for Safe Delivery of Anti-Cancer Drugs. *Sci. Rep.* **2024**, *14*, 5321.
(8) Sharma, Y.; Ohl, C.-D.; Rosselló, J. M. Nanobubble Nucleation by Pulsed Laser Illumination of Colloidal Gold Nanoparticles. *Sci. Rep.* **2024**, *14*, 30491.
(9) Huang, D.; Quan, X.; Cheng, P. An Analysis on Heterogeneous Bubble Nucleation around a Nanoparticle Based on Density Functional Approach. *Int. Commun. Heat Mass Transfer* **2018**, *93*, 66−73.
(10) Volmer, M.; Weber, A. Keimbildung in Übersättigten Gebilden. *Z. Phys. Chem.* **1926**, *119U*, 277−301.
(11) Farkas, L. Keimbildungsgeschwindigkeit in übersättigten Dämpfen. *Z. Phys. Chem.* **1927**, *125U* (1), 236−242.
(12) Becker, R.; Döring, W. Kinetische Behandlung der Keimbildung in übersättigten Dämpfen. *Ann. Phys.* **1935**, *416* (8), 719−752.
(13) Ishida, N.; Inoue, T.; Miyahara, M.; Higashitani, K. Nano Bubbles on a Hydrophobic Surface in Water Observed by Tapping-Mode Atomic Force Microscopy. *Langmuir* **2000**, *16* (16), 6377−6380.
(14) Yang, J.; Duan, J.; Fornasiero, D.; Ralston, J. Very Small Bubble Formation at the Solid-Water Interface. *J. Phys. Chem. B* **2003**, *107* (25), 6139−6147.
(15) Zhang, L.; Zhang, Y.; Zhang, X.; et al. Electrochemically Controlled Formation and Growth of Hydrogen Nanobubbles. *Langmuir* **2006**, *22*, 8109−8113.
(16) Switkes, M.; Ruberti, J. W. Rapid Cryofixation/Freeze Fracture for the Study of Nanobubbles at Solid-Liquid Interfaces. *Appl. Phys. Lett.* **2004**, *84*, 4759−4761.
(17) Martinez, J.; Stroeve, P. Transient Behavior of the Hydrophobic Surface/Water Interface: From Nanobubbles to Organic Layer. *J. Phys. Chem. B* **2007**, *111*, 14069−14072.
(18) Strey, R.; Wagner, P. E.; Schmeling, T. Homogeneous Nucleation Rates for n-Alcohol Vapors Measured in a Two-Piston Expansion Chamber. *J. Chem. Phys.* **1986**, *84*, 2325−2335.
(19) Iland, K.; Wölk, J.; Strey, R.; Kashchiev, D. Argon Nucleation in a Cryogenic Nucleation Pulse Chamber. *J. Chem. Phys.* **2007**, *127*, 154506.
(20) Qiu, C.; Zhang, H. Effects of System Pressure and Heat Flux on Bubble Nucleation and Growth. *Chin. J. Mech. Eng.* **2015**, *28* (5), 964−970.
(21) Liu, H.; Deng, W.; Ding, P.; Zhao, J. Investigation of the Effects of Surface Wettability and Surface Roughness on Nanoscale Boiling Process Using Molecular Dynamics Simulation. *Nucl. Eng. Des.* **2021**, *382*, 111400.
(22) Zhou, W.; Han, D.; Ma, H.; Hu, Y.; Xia, G. Microscopic Mechanisms behind Nucleate Boiling Heat Transfer Enhancement on Large-Aspect-Ratio Concave Nanostructured Surfaces for Two-Phase Thermal Management. *Int. J. Heat Mass Transfer* **2022**, *195*, 123136.
(23) Li, Y.; Zhou, W.; Zhang, Y.; Qi, B.; Wei, J. A Molecular Dynamics Study of Surface Wettability Effects on Heterogeneous Bubble Nucleation. *Int. Commun. Heat Mass Transfer* **2020**, *119*, 104991.
(24) Deng, W.; Ma, S.; Li, W.; Liu, H.; Zhao, J. A. Molecular Dynamics Investigation of Boiling Heat Transfer over Wettability Thermo-Responsive Surface. *Int. J. Heat Mass Transfer* **2022**, *191*, 122856.
(25) Wang, Y.-H.; Wang, S.-Y.; Lu, G.; Wang, X.-D. Explosive Boiling of Nano-Liquid Argon Films on High Temperature Platinum Walls: Effects of Surface Wettability and Film Thickness. *Int. J. Therm. Sci.* **2018**, *132*, 610−617.
(26) Guo, C.; Ji, C.; Kong, Y.; Liu, Z.; Guo, L.; Yang, Y. The Effect of Liquid−Solid Interactions upon Nucleate Boiling on Rough Surfaces: Insights from Molecular Dynamics. *Materials* **2023**, *16*, 1984.
(27) Chen, Y.-J.; Lu, W.; Yu, B.; Tao, W.-Q.; Zhou, W.; Cao, Q. A. Revised Lennard-Jones Potential for Bubble Nucleation Study of Argon Based on the Molecular Dynamics Simulation Method. *J. Mol. Liq.* **2023**, *371*, 121094.
(28) Hu, H.; Lu, Y.; Guo, L.; Chen, X.; Wang, Q.; Wang, J.; Li, Q. Effects of System Pressure on Nucleate Boiling: Insights from Molecular Dynamics. *J. Mol. Liq.* **2024**, *402*, 124745.
(29) Zhou, W.; Han, D.; Ma, H.; Hu, Y.; Xia, G. Molecular Dynamics Study on Enhanced Nucleate Boiling Heat Transfer on Nanostructured Surfaces with Rectangular Cavities. *Int. J. Heat Mass Transfer* **2022**, *191*, 122814.
(30) Wang, W.; Zhang, H.; Tian, C.; Meng, X. Numerical Experiments on Evaporation and Explosive Boiling of Ultra-Thin Liquid Argon Film on Aluminum Nanostructure Substrate. *Nanoscale Res. Lett.* **2015**, *10*, 158.
(31) Wang, Z.; Ye, T.; Guo, K.; Tian, W.; Qiu, S.; Su, G. The Evaporation of Nanoscale Sodium Liquid Film on the Non-Ideal

Nanostructure Surface: A Molecular Dynamics Study. *Int. J. Adv. Nucl. React. Des. Technol.* **2023**, *5*, 1−8.
(32) Zhang, L.; Yang, Y.; Han, J. Microscopic Mechanism of Effects of Nanostructure Morphology on Bubble Nucleation: A Molecular Dynamics Simulation. *Numer. Heat Transfer, Part A* **2024**, *85*, 187−202.
(33) Gao, D.; Sun, Z.; Han, J.; Liu, Z.; Zhao, C.; Bo, H. Geometric Effects on Boiling Heat Transfer Performance: A Molecular Dynamics Study. *Int. J. Heat Fluid Flow* **2024**, *110*, 109599.
(34) Liu, H.; Ahmad, S.; Chen, J.; Zhao, J. Molecular Dynamics Study of the Nanoscale Boiling Heat Transfer Process on Nanostructured Surfaces. *Int. Commun. Heat Mass Transfer* **2020**, *119*, 104963.
(35) Yin, X.; Hu, C.; Bai, M.; Lv, J. An Investigation on the Heat Transfer Characteristics of Nanofluids in Flow Boiling by Molecular Dynamics Simulations. *Int. J. Heat Mass Transfer* **2020**, *162*, 120338.
(36) Li, D.; Jiang, C.; Cao, X.; Li, H.; Hekmatifar, M.; Sabetvand, R. Effect of cross-sectional area and number of Fe nanoparticles on the thermal behavior of pool boiling heat transfer of the water-based nanofluid: A molecular dynamics study. *Case Stud. Therm. Eng.* **2022**, *36*, 102242.
(37) Zhong, Z.; Huang, C.; Wang, X. Enhanced pool boiling heat transfer of multilayer copper-nanoparticle-packed beds by copper mesh coating. *Int. J. Therm. Sci.* **2023**, *184*, 107965.
(38) Yin, X.; Hu, C.; Bai, M.; Lv, J. Molecular Dynamics Simulation on the Effect of Nanoparticles on the Heat Transfer Characteristics of Pool Boiling. *Numer. Heat Transfer, Part B: Fundam* **2018**, *73* (2), 94−105.
(39) Wang, Z.; Li, L. Boiling Heat Transfer of Nanofluids on the Graphene Membrane: A Molecular Dynamics Simulation. *Appl. Therm. Eng.* **2022**, *213*, 118708.
(40) Wang, Y.-H.; Wang, S.-Y.; Lu, G.; Wang, X.-D. Effects of Wettability on Explosive Boiling of Nanoscale Liquid Films: Whether the Classical Nucleation Theory Fails or Not? *Int. J. Heat Mass Transfer* **2019**, *132*, 1277−1283.
(41) Liu, H.; Zhang, L.; Huang, J.; Mao, J.; Chen, Z.; Mao, Q.; et al. Smart Surfaces with Reversibly Switchable Wettability: Concepts, Synthesis and Applications. *Adv. Colloid Interface Sci.* **2022**, *300*, 102584.
(42) Cui, C.; Liu, G.; Gao, H.; Wang, M.; Gao, J. Spiropyran-Based Photo- and Thermal-Responsive Smart Polymer with Controllable Wettability. *Polymer* **2022**, *253*, 124995.
(43) Chen, K.; Jia, J.; Zhao, Y.; Lv, K.; Wang, C. Transparent Smart Surface with pH-Induced Wettability Transition between Superhydrophobicity and Underwater Superoleophobicity. *Mater. Des.* **2017**, *135*, 69−76.
(44) Hu, C.; Pei, Z.; Shi, L.; Tang, D.; Bai, M. Phase change properties of thin liquid films with various thickness on different wettability surfaces. *SSRN Electron. J.* **2022**, 23.
(45) Rony, M. D.; Islam, Md. A.; Thakur, M. S. H.; Islam, M.; Hasan, M. N. Molecular Dynamics Data-Driven Study of Leidenfrost Phenomena in Context to Liquid Thin Film Phase Transformation. *Int. J. Heat Mass Transfer* **2023**, *209*, 124107.
(46) Rabbi, K. F.; Tamim, S. I.; Faisal, A. H. M.; Mukut, K. M.; Hasan, M. N. A Molecular Dynamics Study on Thin Film Liquid Boiling Characteristics under Rapid Linear Boundary Heating: Effect of Liquid Film Thickness. *AIP Conf. Proc.* **2017**, *1851*, 020102.
(47) Bai, P.; Zhou, L.; Du, X. Effects of Liquid Film Thickness and Surface Roughness Ratio on Rapid Boiling of Water over Copper Plates. *Int. Commun. Heat Mass Transfer* **2021**, *120*, 105036.
(48) Liu, X.; Yu, Y.; Hou, C.; Ding, J. Effects of the Wall Temperature on the Boiling Process and the Molecular Dynamics Behavior of the Liquid Hydrogen on a Flat Aluminum Wall. *Int. J. Hydrogen Energy* **2024**, *51*, 1130−1141.
(49) Ilic, M.; Stevanovic, V. D.; Milivojevic, S.; Petrovic, M. M. Explosive Boiling of Water Films Based on Molecular Dynamics Simulations: Effects of Film Thickness and Substrate Temperature. *Appl. Therm. Eng.* **2023**, *220*, 119749.
(50) Zhao, H.; Zhou, L.; Du, X. A. Molecular Dynamics Study of Thin Water Layer Boiling on a Plate with Mixed Wettability and Nonlinearly Increasing Wall Temperature. *J. Mol. Liq.* **2024**, *405*, 125014.
(51) Wu, L.-F.; Tang, Y.-Z.; Ma, L.-X.; Feng, S.-Y.; He, Y. Molecular Dynamics Simulation Study on Nanofilm Boiling of Water with Insoluble Gas. *Int. J. Therm. Sci.* **2022**, *171*, 107212.
(52) Lin, X.-W.; Zhu, X.-G.; Zhou, Z.-F.; Zhu, H.; Ben, N.-Y.; Wang, X.-D.; et al. Molecular Dynamics Simulation on Phase Transition Behaviors of R410A Liquid Film over Solid Copper Surface. *J. Mol. Liq.* **2023**, *383*, 122044.
(53) Tang, Y.; Zhang, X.; Lin, Y.; Xue, J.; He, Y.; Ma, L. Molecular Dynamics Simulation of Nanofilm Boiling on Graphene-Coated Surface. *Adv. Theory Simul.* **2019**, *2*, 1900065.
(54) Tang, Y.-Z.; Meng, X.-W.; Ma, L.-X.; Xue, J.; He, Y. Molecular Dynamics Simulation of Nanofilm Boiling on Atomically Smooth Solid Surface. *Mater. Res. Express* **2019**, *6*, 0850h1.
(55) Chen, Y.; Zou, Y.; Sun, D.; Wang, Y.; Yu, B. Molecular Dynamics Simulation of Bubble Nucleation on Nanostructure Surface. *Int. J. Heat Mass Transfer* **2018**, *118*, 1143−1151.
(56) Chen, Y.; Chen, X.; Yu, B.; Zou, Y.; Tao, W. Molecular Dynamics Study of Bubble Nucleation on an Ideally Smooth Substrate. *Langmuir* **2020**, *36*, 13725−13734.
(57) Cao, Q.; Cui, Z.; Shao, W. Optimization Method for Grooved Surface Structures Regarding the Evaporation Heat Transfer of Ultrathin Liquid Films at Nanoscale. *Langmuir* **2020**, *36*, 2802−2815.
(58) Shahmardi, A.; Tammisola, O.; Chinappi, M.; Brandt, L. Effects of Surface Nanostructure and Wettability on Pool Boiling: A Molecular Dynamics Study. *Int. J. Heat Mass Transfer* **2021**, *167*, 106980.
(59) Deng, X.; Xu, X.; Huang, Y.; Duan, Y.; Liu, C.; Dang, C. A Novel Constant Pressure Control Method for Nucleation Boiling of CO2/Lubricant in Molecular Dynamics Simulation. *Int. J. Refrig.* **2024**, *158*, 35−46.
(60) Lin, X.-W.; Xiang, L.-F.; Zhou, Z.-F.; Zhao, H. Pressure-Controlled Molecular Dynamics Study on the Heterogeneous Nucleation Mechanisms of Dielectric Fluid R1336mzz(Z). *Appl. Therm. Eng.* **2025**, *279*, 127538.
(61) Zhou, K.; Xuan, Y.; Hu, D.; Li, Q. Software Cooling Approach Enables Efficient and Cost-Effective Thermal Management of Multicore Systems. *Int. J. Heat Mass Transfer* **2025**, *244*, 126937.
(62) Kong, D.; Kwon, H.; Jang, B.; Kwon, H.-J.; Asheghi, M.; Goodson, K. E.; Lee, H. Extreme Heat Flux Cooling from Functional Copper Inverse Opal-Coated Manifold Microchannels. *Energy Convers. Manag.* **2024**, *315*, 118809.
(63) Liu, P.; Liu, Y. Thermo-Hydraulic Performance Analysis of Staggered Porous-Solid Microchannel Heat Sinks for High Heat Flux Micro-Electronics Cooling. *Int. J. Heat Mass Transfer* **2026**, *254*, 127675.
(64) Petelin, J.; Marš, M.; Mur, J.; Petkovšek, R. In-Situ Measurements of Residual Heating during Pulse-On-Demand Femtosecond Laser Surface Microprocessing. *Opt. Laser Technol.* **2025**, *190*, 113201.
(65) Goodarzi, R.; Razzaghi, D.; Hajiesmaeilbaigi, F. Linear Chirping Effects on Heating of Silicon Surface after Interaction with Femtosecond Laser Pulses. *Optik - Int. J. Light Electron Opt.* **2020**, *202*, 163480.
(66) Chen, L.; Zhu, Y.; Huang, H.; Zhou, D.; Peng, K.; Wang, Y. Process-Surface Topography-Tribological Performance of Surface Micro-Textures by Nanosecond Laser Ablation with Low-Melting Alloy Coatings. *Tribol. Int.* **2026**, *214*, 111167.
(67) Amaral, M. N.; Kumar, P.; Faísca, P.; Ferreira, H. A.; Coelho, J. M. P.; Gaspar, M. M.; Reis, C. P. Gold Nanoparticle-Mediated Photothermal Therapy: Expanding the Frontiers of Cancer Treatment and Theragnostics. *Biomed. Pharmacother.* **2025**, *190*, 118399.
(68) Liu, J.; Yu, X.; Luo, X.; Yang, Z.; Zhang, N.; Ning, S.; Wang, C. Nanoparticle and Photothermal Mediated Mesenchymal-Epithelial Transition in Cancer Cells to Slow Cancer Cell Migration. *Chem. Eng. J.* **2025**, *517*, 164286.

https://doi.org/10.1021/acs.langmuir.5c06175
Langmuir 2026, 42, 7212−7227

(69) Shirisha, N.; Sonker, A.; Ramesh, J. V. N.; Saidani, T.; Rajesh, Y.; Vydehi, K. Optimizing Thermal Dose Prediction in Nanoparticle-Mediated Photothermal Therapy Using a Convolutional Neural Network-Based Model. *J. Therm. Biol.* **2025**, *128*, 104076.
(70) Chen, Y.; Yu, B.; Zou, Y.; Chen, B.; Tao, W. Molecular Dynamics Studies of Bubble Nucleation on a Grooved Substrate. *Int. J. Heat Mass Transfer* **2020**, *158*, 119850.
(71) Zhao, H.; Zhou, L.; Du, X. Bubble Nucleation on Grooved Surfaces with Hybrid Wettability: Molecular Dynamics Study under a Transient Temperature Boundary Condition. *Int. J. Heat Mass Transfer* **2021**, *166*, 120752.
(72) Bai, P.; Zhou, L.; Du, M.; Wang, D.; Liu, Y.; Du, X. Recent Advances in Molecular Dynamics Research on Nanoscale Boiling Heat Transfer. *Renew. Sustain. Energy Rev.* **2025**, *222*, 115955.
(73) Chen, Y.; Li, J.; Yu, B.; Sun, D.; Zou, Y.; Han, D. Nanoscale Study of Bubble Nucleation on a Cavity Substrate Using Molecular Dynamics Simulation. *Langmuir* **2018**, *34*, 14234−14248.
(74) Rahman, A. Correlations in the Motion of Atoms in Liquid Argon. *Phys. Rev.* **1964**, *136*, A405−A411.
(75) Vrabec, J.; Kedia, G. K.; Fuchs, G.; Hasse, H. Comprehensive Study of the Vapour−Liquid Coexistence of the Truncated and Shifted Lennard−Jones Fluid Including Planar and Spherical Interface Properties. *Mol. Phys.* **2006**, *104*, 1509−1527.
(76) MacDowell, L. G.; Blas, F. J. Surface Tension of Fully Flexible Lennard-Jones Chains: Role of Long-Range Corrections. *J. Chem. Phys.* **2009**, *131*, 074705.
(77) Nakanishi, K.; Toukubo, K. Molecular Dynamics Studies of Lennard-Jones Liquid Mixtures. V. Local Composition in Several Kinds of Equimolar Mixtures with Different Combining Rule. *J. Chem. Phys.* **1979**, *70*, 5848−5850.
(78) Cao, Q.; Li, Z.; Cui, Z. Nanoscale Investigation of Bubble Nucleation and Boiling on Random Rough Surfaces. *Langmuir* **2023**, *39*, 12754−12761.
(79) Liao, M.-J.; Duan, L.-Q. Effect of the Hybrid Hydrophobic-Hydrophilic Nanostructured Surface on Explosive Boiling. *Coatings* **2021**, *11*, 212.
(80) Verlet, L. Computer "Experiments" on Classical Fluids. I. Thermodynamical Properties of Lennard-Jones Molecules. *Phys. Rev.* **1967**, *159*, 98−103.
(81) Hossain, A.; Miah, M. N.; Hasan, M. A Molecular Dynamics Study on Thin Film Phase Change Characteristics over Nano-Porous Surfaces with Hybrid Wetting Conditions. *Int. Commun. Heat Mass Transfer* **2024**, *156*, 107599.
(82) Tegeler, C.; Span, R.; Wagner, W. A New Equation of State for Argon Covering the Fluid Region for Temperatures from the Melting Line to 700 K at Pressures up to 1000 MPa. *J. Phys. Chem. Ref. Data* **1999**, *28*, 779−850.
(83) Nicolas, J. J.; Gubbins, K. E.; Streett, W. B.; Tildesley, D. J. Equation of State for the Lennard-Jones Fluid. *Mol. Phys.* **1979**, *37*, 1429−1454.
(84) Debenedetti, P. G. *Metastable Liquids: Concepts and Principles*; Princeton University Press: Princeton, NJ, 1996.
(85) Deng, W.; Ahmad, S.; Liu, H.; Chen, J.; Zhao, J. Improving Boiling Heat Transfer with Hydrophilic/Hydrophobic Patterned Flat Surface: A Molecular Dynamics Study. *Int. J. Heat Mass Transfer* **2022**, *182*, 121974.
(86) Zhang, K.; Yang, J.; Huai, X. Surface Topography Controls Bubble Nucleation at Rough Water/Silicon Interfaces for Different Initial Wetting States. *Int. J. Heat Mass Transfer* **2024**, *224*, 125323.
(87) Zhang, L.; Xu, J. Nucleate Boiling of Thin Liquid Films on Nanostructured Surfaces with Hybrid Wettability Using Molecular Dynamics Simulation. *J. Mol. Liq.* **2022**, *366*, 120272.
(88) Chen, Y.; Zou, Y.; Wang, Y.; Han, D.; Yu, B. Bubble Nucleation on Various Surfaces with Inhomogeneous Interface Wettability Based on Molecular Dynamics Simulation. *Int. Commun. Heat Mass Transfer* **2018**, *98*, 135−142.
(89) Li, Z.; Wang, Z.; Shao, W.; Cao, Q.; Cui, Z. Ultrathin Liquid Film Nucleate Boiling on Grooved Surfaces with Variational Aspect Ratio. *Thermal Sci. Eng. Prog.* **2023**, *43*, 102023.
(90) Nagayama, G.; Tsuruta, T.; Cheng, P. Molecular Dynamics Simulation on Bubble Formation in a Nanochannel. *Int. J. Heat Mass Transfer* **2006**, *49*, 4437−4443.
(91) Kashchiev, D. *Nucleation: Basic Theory with Applications*; Butterworth-Heinemann: Oxford, 2000.
(92) Kelton, K. F.; Greer, A. L. *Nucleation in Condensed Matter: Applications in Materials and Biology*; Elsevier: Amsterdam, 2010.
(93) Savitzky, A.; Golay, M. J. E. Smoothing and Differentiation of Data by Simplified Least Squares Procedures. *Anal. Chem.* **1964**, *36*, 1627−1639.
(94) Guan, S. Y.; Zhang, Z. H.; Wu, R.; Gu, X. K.; Zhao, C. Y. Boiling on Nano-Porous Structures: Theoretical Analysis and Molecular Dynamics Simulations. *Int. J. Heat Mass Transfer* **2022**, *191*, 122848.
(95) Green, D. W.; Perry, R. H. *Perry's Chemical Engineers' Handbook*, 8 ed.; McGraw-Hill: New York, 2007; . th ed..
(96) Li, Z.; Lou, J.; Wu, X.; Li, X.; Chang, F.; Wang, H.; Li, H. Molecular Dynamics Study on Bubble Nucleation Characteristics on Rectangular Nano-Grooved Surfaces. *J. Mol. Liq.* **2025**, *420*, 126836.

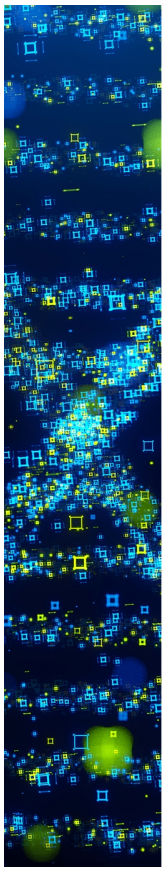
CAS BIOFINDER DISCOVERY PLATFORM™
STOP DIGGING THROUGH DATA —START MAKING DISCOVERIES
CAS BioFinder helps you find the right biological insights in seconds
Start your search
CAS
A division of the American Chemical Society

https://doi.org/10.1021/acs.langmuir.5c06175
Langmuir 2026, 42, 7212−7227